Testing the Limits and Breakdown of the Non-Acceleration Theorem for Orographic Stationary Waves

Nicholas J. Lutsko*

Scripps Institution of Oceanography, University of California at San Diego, La Jolla, CA, USA

* *Corresponding author address:* Nicholas Lutsko, nlutsko@ucsd.edu

E-mail: nlutsko@ucsd.edu

ABSTRACT

The non-acceleration theorem states that the torque exerted on the atmosphere by orography is exactly balanced by the convergence of momentum by the stationary waves which the orography excites. This balance is tested in simulations with a stationary wave model and with a dry, idealized general circulation model (GCM), in which large-scale orography is placed at the latitude of maximum surface wind speed. For the smallest mountain considered (maximum height $H = 0.5$m), the non-acceleration theorem nearly holds, but the damping in the stationary wave model induces an offset between the stationary eddy momentum flux (EMF) convergence and the mountain torque, leading to residual mean flow changes. A stationary non-linearity appears for larger mountains ($H \geq$10m), driven by preferential deflection of the flow around the poleward flank of the orography, and causes further breakdown of the non-acceleration balance. The non-linearity grows as H is increased, and is stronger in the GCM than in the stationary wave model, likely due to interactions with transient eddies. The mid-latitude jet shifts poleward for $H \leq$ 2km and equatorward for larger mountains, reflecting changes in the transient EMFs, which push the jet poleward for smaller mountains and equatorward for larger mountains. The stationary EMFs consistently force the jet poleward. These results add to our understanding of how orography affects the atmosphere's momentum budget, providing insight into how the non-acceleration theorem breaks down; the roles of stationary non-linearities and transients; and how orography affects the strength and latitude of eddy-driven jets.

1. Introduction

Orography plays a fundamental role in shaping the dynamics of the atmosphere. At small scales (10s-100s km), air flow over mountains generates internal gravity waves, which propagate vertically and horizontally, transporting momentum away from their source and depositing it wherever they break. Alternatively, if the flow is too slow to move up and over the orography, flow-splitting may occur, producing long, persistent downstream wakes. Parameterizing these and other impacts of small-scale orography is notoriously difficult, yet is essential for making accurate weather forecasts and for predicting future circulation changes (see Sandu et al. (2019) for a recent review).

At larger scales, orographically-forced quasi-stationary planetary waves transport substantial amounts of heat, moisture and momentum through the atmosphere, exerting a strong control on regional climates and also playing a key role in the zonal-mean circulation. Our understanding of stationary waves is based on linear theory, which provides good qualitative agreement with observations in many respects. For example, the Charney-Eliassen model, which approximates the atmosphere as a barotropic, quasi-geostrophic fluid in a β-plane channel, does a reasonable job of reproducing the observed Northern Hemisphere wintertime stationary wave pattern when forced with observed orography (Charney and Eliassen (1949); Held (1983)). However, there are a number of open questions concerning linear theory's relevance for quantitatively understanding observed large-scale stationary wave patterns. These include the role of non-linear interactions between stationary waves (Wang and Kushner 2010), and how to account for interactions between stationary waves and transient eddies. Past modeling studies have found that transients damp the stationary wave response to orography (Vallis and Roads 1984) or that orographically-forced stationary waves are unaffected by the presence of transients (Nigam et al. 1988), and it is still unclear how to account for transient eddies in linear stationary wave theory. Another issue concerns stationary non-linearities: when the linear approximations break down (Cook and Held (1992); Lutsko and Held (2016)), how to best account for stationary non-linearities (e.g., Trenberth and Chen (1988); Valdes and Hoskins (1991)) and how relevant they are for the observed atmospheric circulation.

One question which has received less attention recently is how orographically-forced stationary waves affect the zonal-mean circulation. Early stationary wave studies typically considered channel geometries, in which waves can only propagate zonally and vertically (e.g., Charney and Eliassen (1949); Smagorinsky (1953); Saltzman (1963); Saltzman (1965); Kasahara (1966); Derome and Wiin-Nielsen (1971); Egger (1978)). Resonances appear generically in this setting, which leads to the existence of multiple equilibrium states when coupling to the mean flow is included, with, for instance, a large stationary wave amplitude/weak mean flow state co-existing with a small stationary wave amplitude/strong mean flow state for a given mountain height and shape (Charney and DeVore 1979).

The realization that stationary waves tend to propagate (approximately) along great circles (Hoskins et al. (1977); Grose and Hoskins (1979); Hoskins and Karoly (1981)) shifted the emphasis away from the coupled wave-mean flow problem and towards understanding the propagation of orographic waves, particularly their interactions with subtropical critical layers. Stationary waves may be absorbed, reflected or over-reflected by critical layers (Killworth and McIntyre 1985), though the fact that the climatological stationary eddy momentum flux is directed from the tropics towards midlatitudes suggests that on average these waves are absorbed, rather than reflected. In practice, it seems difficult to create a reflecting critical layer for systems resembling the real atmosphere, with transient eddies and a Hadley circulation (though see Walker and Magnusdottir (2003)).

A separate series of papers have investigated the ability of mid-latitude jets to act as waveguides for stationary waves (Branstator (1983); Hoskins and Ambrizzi (1993); Branstator (2002); Branstator and Selten (2009); Manola et al. (2013); Petoukhov et al. (2013); Saeed et al. (2014); Lutsko and Held (2016)). "Circumglobal" waves that are trapped in these waveguides can propagate over long zonal distances with little meridional motion, and may play an important role in the atmosphere's response to increased CO_2 concentrations (Brandefelt and Kornich (2008); Simpson et al. (2016)).

All of these studies have taken the mean flow as fixed, and then examined stationary wave propagation under a given mean flow (see also Wills and Schneider (2018)). But the momentum transported by stationary waves plays a key role in the dynamics of mid-latitude jets and storm-tracks (e.g., Kaspi and Schneider (2013)), and changes in wave properties, such as a transition from a meridionally-trapped wave to a meridionally-propagating wave can potentially lead to large changes in stationary eddy momentum fluxes (EMFs), driving jet shifts or changes in jet intensity. As an example, White et al. (2017) found that the combined effects of the Himalayas and the Tibetan Plateau force relatively small amplitude stationary waves that are trapped within a waveguide and therefore have little impact on the jet over eastern Asia and the Pacific. By contrast, the Mongolian mountains, which are further north excite stronger waves that propagate meridionally and intensify the Pacific jet. An externally-driven shift of the jet could alter these different wave-paths, which could in turn amplify or damp the initial jet shift.

Through the non-acceleration theorem, linear theory says that stationary EMFs should balance the torque exerted by the mountain on the atmosphere (see following subsection), however this balance is not typically seen in simulations[1]. Manabe and Terpstra (1974) compared simulations of a GCM with and without topography, and saw an increase in the transient EMF when topog-

[1] White (1986) investigated a non-linear extension of the non-acceleration theorem to a quasi-geostrophic system.

raphy is removed (Park et al. (2013) found a similar compensation between the stationary and transient eddy heat fluxes); while Cook and Held (1992) found that in an idealized, moist GCM the mountain torque is mostly balanced by a reduction in the surface friction. Past studies have found that orography exerts a strong drag on zonal jets (e.g., Brayshaw et al. (2009)) and that orography can accelerate jets (Son et al. (2009); White et al. (2017)). Thus the question of how the atmosphere balances stationary eddy momentum transport, and in particular how the strengths and latitudes of eddy-driven jets respond to the presence of orography, is an open question.

In this study, the response of the angular momentum budget of an idealized, dry general circulation model (GCM) to orography is systematically investigated, through a series of simulations in which the height of the orography is increased. These include simulations with the full dynamical GCM, and simulations in which the GCM is converted into a stationary wave model, which does not include transient eddies and so is the most likely setting for the non-acceleration theorem to hold. Together, these simulations are used to investigate how the atmosphere responds to the stationary EMFs induced by the presence of orography, how this response differs from what is expected from the non-acceleration theorem and how the response is affected by the presence of transient eddies. The goals are to provide a better understanding of the practical utility of the non-acceleration theorem, including how transients and stationary non-linearities affect the non-acceleration balance, and to further investigate how large orography affects the strength and latitude of mid-latitude jets.

The paper is structured as follows: after reviewing the non-acceleration theorem for orographically-forced stationary waves in the following subsection, the GCM and the stationary wave model are described in section 2. The momentum budget of the unperturbed system is then presented in section 3, and the stationary wave model results are discussed in section 4 and the

GCM simulations with small orography in section 5. The GCM experiments with large orography are presented in section 6, and then conclusions are given in section 7.

a. The non-acceleration theorem for orographic stationary waves

The non-acceleration theorem says that, in the absence of friction, and neglecting the effects of transient eddies, the torque exerted on the atmosphere by orography is exactly balanced by the convergence of momentum by the stationary waves which the orography excites[2]. Consider the eddy potential vorticity (PV) equation for an inviscid, adiabatic, continuous quasi-geostrophic (QG) system, linearized about a zonal-mean flow $\bar{u}$:

$$\frac{\partial q^*}{\partial t} + \bar{u}\frac{\partial q^*}{\partial x} + v^*\frac{\partial \bar{q}}{\partial y} = 0, \tag{1}$$

where $q^* = \nabla^2\psi^* + \frac{f_0^2}{\rho}\frac{\partial}{\partial z}\left(\frac{\rho}{N^2}\frac{\partial \psi^*}{\partial z}\right)$ is the eddy PV, v^* is the eddy meridional wind and $\frac{\partial \bar{q}}{\partial y} = \beta - \frac{\partial^2 \bar{u}}{\partial y^2} - \frac{f_0^2}{\rho}\frac{\partial}{\partial z}\left(\frac{\rho}{N^2}\frac{\partial \bar{u}}{\partial z}\right)$ is the zonal-mean meridional PV gradient. ψ^* is the eddy streamfunction, f_0 is a reference value of the Coriolis parameter, ρ is density and N^2 is the buoyancy frequency. The vertical co-ordinate $z = H\ln(p_s/p)$, where H is the scale-height of the atmosphere, p is pressure and p_s is surface pressure. The surface boundary condition is the QG thermodynamic equation at $z = 0$

$$\frac{\partial}{\partial t}\left(\frac{\partial \psi^*}{\partial z}\right) + \bar{u}\frac{\partial}{\partial x}\left(\frac{\partial \psi^*}{\partial z}\right) - v^*\frac{\partial \bar{u}}{\partial z} = -\frac{N^2}{f_0}w, \tag{2}$$

and the lower boundary condition on the vertical velocity is

$$w(z=0) = -\frac{\partial}{\partial t}\left(\frac{f_0}{g}\psi^*\right) + \bar{u}\frac{\partial h}{\partial x}, \tag{3}$$

[2]Note that for transient eddies, the non-acceleration theorem says that the transient eddy momentum flux convergence balances the form drag exerted by one layer on another.

where h is the height of the mountain and g is the gravitational constant. Substituting 3 into 2 and re-arranging then gives

$$\frac{\partial}{\partial t}\left(\frac{\partial \psi^*}{\partial z} - \frac{N^2}{g}\psi^*\right) + \bar{u}\frac{\partial}{\partial x}\left(\frac{\partial \psi^*}{\partial z}\right) - v^*\frac{\partial \bar{u}}{\partial z} = -\frac{N^2}{f_0}\bar{u}\frac{\partial h}{\partial x} \quad \text{at } z = 0. \tag{4}$$

Multiplying equation 1 by q^*, equation 4 by $s^* = \frac{\partial \psi^*}{\partial z} + \frac{N^2}{f_0}h$ and taking zonal-means gives

$$\frac{1}{2}\frac{\partial \overline{q^{*2}}}{\partial t} = -\overline{v^*q^*}\frac{\partial \bar{q}}{\partial y}, \quad \text{for } z > 0, \tag{5a}$$

$$\frac{1}{2}\frac{\partial \overline{s^{*2}}}{\partial t} - \frac{N^2}{g}\overline{s^*\frac{\partial \psi^*}{\partial t}} = \overline{v^*s^*}\frac{\partial \bar{u}}{\partial z} = -\overline{v^*s^*}\frac{\partial \bar{s}}{\partial y}. \quad \text{at } z = 0. \tag{5b}$$

The left hand sides of these equations are zero for a steady wave and so $\overline{v^*q^*} = \overline{v^*s^*} = 0$.

In the Transformed Eulerian Mean formulation the zonal momentum equation is (Andrews and McIntyre 1976)

$$\frac{\partial \bar{u}}{\partial t} = \overline{v^*q^*} + f_0\overline{v^R}, \tag{6}$$

where $\overline{v^R}$ is the residual velocity

$$\overline{v^R} = \bar{v} - \frac{f_0}{\rho}\frac{\partial}{\partial z}\left(\frac{\rho}{N^2}\overline{v^*\frac{\partial \psi^*}{\partial z}}\right).$$

Integrating the momentum equation vertically and using a radiation condition at infinity then gives

$$0 = \left\langle \overline{v^*q^*} \right\rangle = -\left\langle \frac{\partial \overline{u^*v^*}}{\partial y} \right\rangle + \frac{f_0^2}{N^2}\overline{v^*\frac{\partial \psi^*}{\partial z}}(0), \tag{7}$$

where angle brackets denote vertical integrals. From before,

$$\overline{v^*s^*}(0) = \overline{v^*\frac{\partial \psi^*}{\partial z}}(0) + \frac{N^2}{f_0}\overline{v^*h} = 0,$$

hence

$$\overline{v^*\frac{\partial \psi^*}{\partial z}}(0) = -\frac{N^2}{f_0}\overline{v^*h}. \tag{8}$$

Finally, substituting into equation 7 and using geostrophy

$$\underbrace{\left\langle \frac{\partial \overline{u^*v^*}}{\partial y} \right\rangle}_{\text{stationary eddy momentum flux}} = \underbrace{\overline{h\frac{\partial p_s}{\partial x}}}_{\text{mountain torque}}, \tag{9}$$

where p_s is surface pressure.

2. Models and Experiments

a. GCM description and experiments

The GCM simulations are the same simulations as in Lutsko and Held (2016). These were carried out using the GFDL spectral dynamical core, forced by zonally-symmetric Newtonian relaxation to a prescribed equilibrium temperature field and damped by Rayleigh friction near the surface. The parameter settings are the standard Held and Suarez (1994) parameters, with forcing symmetric about the equator. All simulations presented here were run at T42 resolution with 30 evenly spaced sigma levels, and data sampled once per day. A control simulation was integrated for 40 000 days, with the first 2000 days discarded to ensure the model had spun-up.

The orography consists of Gaussian mountains, centered at 90°E and 45°N, with the functional form:

$$h(\phi,\lambda) = H \exp\left\{-\left[\frac{(\phi-45^\circ)^2}{\alpha^2} + \frac{(\lambda-90^\circ)^2}{\beta^2}\right]\right\} \tag{10}$$

where H is the maximum height of the mountain in meters; ϕ and λ are latitude and longitude, respectively; and α and β are half-widths, both set to 15° in the initial perturbation experiments (see also Cook and Held (1992)). The latitude of the orography was chosen to be co-located with the latitude of maximum surface wind speed.

The maximum height of the orography, H, was varied from 250m to 5000m. For heights less than 250m the responses are not clearly separable from the noise. Cases with H less than 1km were run for 40 000 days and the responses were obtained by discarding the first 2000 days of each perturbation experiment and averaging over the rest of the integration. These long integration times were required to ensure that the responses had equilibrated, in the sense that the response calculated using half of the data was indistinguishable from the response calculated using all of the data. This ensures that the stationary wave signal is clearly distinguishable from the transients. Cases with larger mountains equilibrated more quickly and so were only run for 20 000 days.

Lutsko and Held (2016) found that these simulations separated into a "linear" regime, in which the model's response is approximately linear in H, and a non-linear regime, in which the amplitude of the model's response increases sublinearly, with the transition occurring between $H = 700$m and $H = 1$km. Associated with this transition, the stationary wave response transitions from being more zonally-oriented (in the linear regime), to propagating more meridionally in the non-linear regime (compare panels a and b of Figure 1).

b. Stationary wave model and experiments

Following previous studies such as Held et al. (2002) and Chang (2009), the stationary wave model was created by applying strong damping to the same GCM described above and by strongly relaxing the zonal-mean flow to the time- and zonal-mean flow in the control simulation. The results described below come from simulations in which the hyperdiffusion was doubled from 1.157×10^{-4} m^{8}s^{-1} (in the original GCM simulations) to 2.31×10^{-4} m^{8}s^{-1}, and the Rayleigh friction damping times for both the vorticity and divergence equations were set to 0.3, 0.5, 1.0, and 8.0 days at the lowest four σ levels (0.997, 0.979, 0.935 and 0.866), and 15 days throughout the rest of the domain. The Newtonian cooling time-scale was decreased from 40 days (the Held-Suarez value) to 15 days at all levels and the relaxation time-scale of the zonal-mean winds was set to 1 day. These parameter settings were found to successfully eliminate the transients in the model; however, there is no objective method for choosing the optimal parameter settings for creating a stationary wave model, and the simulations were repeated with several different parameter settings to ensure that the results are robust (e.g., the relaxation time-scale of the zonal-mean wind was varied from 0 to 3 days). In all experiments, the stationary wave model was integrated for 200 days and averages were taken over days 50 to 200. Inspection of the flow indicated that the model equilibrates after 15-20 days.

The normalized eddy streamfunction response of the stationary wave model to H = 500m orography (Figure 1c) compares well with the H = 500m simulation with the full GCM (panel a). The patterns of the responses are very similar, though the stationary wave model's response is roughly 25% weaker than the GCM's. This difference is discussed further in section 5.

The stationary wave model has no transient eddies or changes to the mean flow, eliminating two factors which are likely to interfere with the non-acceleration balance. However, it is still possible for the friction to alter the momentum balance, or for a stationary non-linearity to appear. Comparing the stationary wave model results with the full GCM allows the role of transients and mean flow changes to be made clear.

3. Momentum Budget of the Unperturbed Atmosphere

Before discussing the response to orography, the momentum budget of the control simulation is presented here for reference. The steady state, vertically-integrated zonal-mean momentum budget of the GCM can be written as

$$\int_0^{p_s} \frac{dp}{g} \frac{1}{a\cos^2\phi} \frac{\partial}{\partial\phi} \left(\cos^2\phi \left(\overline{[u][v]} + \overline{[u]^*[v]^*} + \overline{[u'v']}\right)\right) + \left[\overline{\frac{p_s}{a\cos\phi} \frac{\partial h}{\partial\lambda}}\right] - [\overline{F}] = 0, \qquad (11)$$

where a is the Earth's radius, F is friction, square brackets are time means, overbars are zonal means, asterisks are deviations from the zonal mean and primes are deviations from the time mean. Throughout this study, the transient term is calculated using the daily zonal-mean surface pressure (recall that data are collected once per day):

$$\left[\int_0^{\overline{p_s(t)}} \frac{dp}{g} \frac{1}{a\cos^2\phi} \frac{\partial}{\partial\phi} \left(\cos^2\phi (\overline{u'v'})\right)\right].$$

The profiles of the terms in the angular momentum budget of the control integration are shown in Figure 2. As expected, the main balance is between the transient EMF convergence and the friction. These are largest at mid-latitudes, where the transient eddies accelerate the flow and the friction decelerates the flow, and change sign in the tropics and at high latitudes. Both terms are small in the subtropics, where the momentum flux by the mean flow is the largest term in the budget (Peixoto and Oort 1992).

4. Stationary Wave Model Results

The stationary wave model was run with mountains of maximum height H = 0.5m, 10m, 500m and 2km. In testing, it was found that H = 0.5m is the smallest mountain height that produces a response distinguishable from the noise in this model set-up; however, it is worth noting how extreme this case is, representing a mountain with roughly the same horizontal extent as the Tibetan plateau but a maximum height of less than one meter.

The normalized mountain torque and stationary EMF convergence are similar in the H = 0.5m and H = 10m experiments (panels a and b of Figure 3), as the torque decelerates the flow between about 30° and 60°, while the stationary EMF convergence accelerates the flow at these latitudes. However, while the torque has a single maximum at 48°N, the stationary EMF convergence has maxima at 42° and 55°. This pattern leads to a slight deceleration of the jet between 40° and 52° (and hence a reduction in the friction at these latitudes, see Figure 3c[3]) and an acceleration between 55°N and 62°N. The stationary EMF convergence also decelerates the flow in the subtropics, between ∼10° and 30°N.

[3]Note that in the stationary wave model the friction is the only other term in the momentum budget, so it balances the residual of the torque and the stationary EMF convergence.

As the height of the mountain is increased, the torque moves equatorward slightly (darker red lines in Figure 3a), though its normalized magnitude is roughly constant, and the latitude of maximum stationary EMF convergence shifts polewards. This is a result of the poleward stationary EMF convergence maximum growing relative to the equatorward maximum as the height is increased, so that for H = 2km there is a single maximum in the EMF convergence at 52°N. This extends the region over which the mean flow is accelerated to 48°N - 62°N, and pushes the jet polewards (Figure 3c).

To understand these response, the left panels of Figure 4 show the horizontal components of the Plumb flux at 350hPa (vectors, see Appendix for how the Plumb flux is calculated) and the vertical component at 800hPa (red contours) for the H = 0.5m experiment (panel a), the H = 10m experiment (panel c) and the H = 500m experiment (panel e). In the H = 0.5m experiment the wave source, as measured by the vertical component of the Plumb flux, is centered slightly northeast of the peak of the orography (Figure 4a). Panel b of Figure 4 shows the anomalous 800hPa wind vectors (green arrows) and the zonal anomalies in θ (filled contours). The wind vectors indicate that the flow is preferentially deflected north of the orography, so that the anticyclone associated with the orographic high is centered north of the mountain peak. There is also a cyclone immediately downstream of the orography, southeast of the anti-cyclone, and weak cooling over the mountain, though this is likely an artifact of the algorithm for interpolating from σ co-ordinates to pressure co-ordinates. The anticyclone/cyclone pair, centered on the northeastern flank of the orography, is responsible for shifting PF_z to the northeast of the orography.

The preferential poleward deflection of the flow is caused by the mean isentropic slope, which slants upward with latitude. Hence air flowing along an isentrope that is deflected equatorward also moves to lower altitudes, and vice-versa for air deflected polewards. This makes the orography appear “taller” on its equatorward flank than on its poleward flank, and more of the air flows polewards around the orography (Valdes and Hoskins 1991).

Returning to Figure 4a, the arrows show that the majority of the wave energy propagates equatorward, and is dissipated by the damping as it propagates into the subtropics, with little evidence of the wave being absorbed near the critical layer, where $u = 0$ (the cyan line). Part of the equatorward propagating wavetrain is also refracted into the waveguide and propagates zonally before being dissipated (the mean flow in this simulation acts as a waveguide for waves with zonal wavenumber $k = 5$; Lutsko and Held (2016)). A smaller portion of the wave energy propagates polewards, where it appears to reflect off a turning latitude and propagate equatorwards, before dissipating or, possibly, being refracted into the waveguide.

The dissipation of the wavetrains as they propagate away from the orography leads to the stationary EMF convergence maximum near 40°N (from the equatorward-moving wavetrain), the smaller maximum near 55°N (from the poleward-moving wavetrain) and to the EMF divergence in the subtropics. So in this small H case, the damping is responsible for the lack of exact compensation between the torque and the stationary EMF convergence, by dissipating the stationary wave as it propagates away from the orography.

There are two wave sources in the H = 10m case (Figure 4c): one to the east and one to the north of the orography. These are associated with negative temperature anomalies over the equatorward flank of the mountain and, more weakly, on the northeast flank of the mountain (panel d). The flow is similar to the H = 0.5m case, though the axis of the anti-cyclone/cyclone pair is rotated further northwest-southeast, rather than the more zonal orientation seen for H = 0.5m. This circulation pattern advects cold air along the eastern and northeastern flanks of the mountain, creating the temperature anomalies. Since the circulation is shifted polewards of the orography, the temperature advection is not balanced by the adiabatic cooling/warming of the air as it rises and sinks over the orography (the flow in the 0.5m case seems to be too weak to induce substantial temperature anomalies).

Plotting each of the terms in PF_z indicates that the temperature anomalies are responsible for the two wave sources, primarily through the $\frac{\partial[\theta^*]}{\partial\lambda}$ term (not shown). Thus the preferential poleward deflection of the flow, and the resulting temperature anomalies, are responsible for generating a stationary non-linearity. The horizontal components of the Plumb flux suggest that the propagation of the wavetrains remains similar to the $H = 0.5$m case, however, as the majority of the wave energy propagates equatorward and is dissipated near the critical line. One difference is that the poleward wave source is close to the turning latitude, and there is less evidence of wave reflection from the turning latitude on the poleward edge of the waveguide. Instead, the poleward wavetrain propagates roughly parallel to the turning latitude, before dissipating. Despite this difference, the net effect for the $H = 10$m case is a similar profile of EMF convergence and divergence as in the $H = 0.5$m case.

The responses to the larger mountains are generally similar to the $H = 10$m case (panels e and f of Figure 4), though the wave sources change shape somewhat, causing the poleward shift of the EMF convergence maximum discussed earlier. The stationary waves are also able to propagate further into the subtropics, and cause the critical layer to be slightly distorted between 100° and 150°E (cyan line in Figure 4e). Finally, the temperature anomalies induced by the flow in the simulations with larger orography cause p_s and $\frac{\partial h}{\partial\lambda}$ to move out of phase and hence shift the mountain torque equatorward (not shown).

5. Response to Small Mountains

The GCM experiments with small ($H <$1km) mountain heights are in an approximately linear regime, with a roughly constant normalized torque (blue curves in Figure 3a) that decelerates the flow over most of the mountain and weakly accelerates the flow between about 55° and 65°N. The normalized stationary EMF convergence is also roughly constant in these simulations (blue curves in Figure 3b), and is shifted polewards of the torque, accelerating the flow between about 40° and 70° and decelerating the flow at lower latitudes (note: the larger EMF convergence for the 333m case (orange curve) is a result of sampling error). A similar poleward displacement of the stationary EMF convergence relative to the torque was seen in the GCM experiments of Cook and Held (1992). Because of this offset, and because the stationary EMF convergence is larger than the torque, the two terms do not cancel (blue curves in Figure 3c), with the residual decelerating the flow equatorward of $\sim$42°N and accelerating the flow poleward of this latitude. This induces a deceleration and poleward shift of the mid-latitude jet (Figure 5), though the responses of the friction, the transient EMFs and the mean flow are comparable to the sampling error for these small mountain heights[4], making it difficult to identify how exactly the momentum budget is balanced in the small H GCM experiments.

The results of the previous section suggest that the poleward displacement of the stationary EMF convergence relative to the torque is partly due to the stationary non-linearity, however the EMFs are larger in the GCM experiments than in the stationary wave model. Comparing panels g and h of Figure 4 with panels e and f demonstrates that the patterns of stationary wave propagation and temperature anomalies are similar in the GCM and the stationary wave model, but that the amplitudes of the wave response and of the temperature anomalies are larger in the GCM. Hence transient eddies appear to amplify the response to orography relative to the stationary wave model, producing larger stationary EMFs and larger potential temperature anomalies over the mountain in the GCM experiments. The propagation of the stationary wave does not differ substantially in the GCM compared to the stationary wave model, implying that mean flow changes are not

[4]I.e., the changes in the hemisphere with the mountain are comparable to the changes in the hemisphere without the mountain

responsible for the changes in the stationary EMFs. The deceleration of the zonal-mean winds in the H = 500m GCM experiment (Figure 5) should weaken the stationary wave source, in contrast to the strengthening seen here.

It is possible that the weaker hyperdiffusion and surface friction in the GCM also contribute to the larger response, however these should mostly affect the wave propagation and the far-field response, and should have less of an impact in the immediate vicinity of the mountain, where the mountain-induced response is larger. In stationary wave model experiments with other parameter settings, the amplitude of the response is relatively insensitive to the strength of the damping, provided the damping is strong enough to eliminate the transient eddies (not shown).

Finally, in addition to the stationary non-linearity discussed in the previous section, another factor which may be responsible for the lack of cancellation between the EMF convergence and the torque is diabatic heating over the mountain: in the Held-Suarez set-up the Newtonian cooling is applied on constant σ-levels, so the near-surface air at the top of the mountain is relaxed to the same temperature as air at sea level (at the same latitude), producing a strong radiative heating over the mountain.

To investigate how orographically-induced diabatic heating affects the model's response, the GCM experiments were repeated with new zonally-varying equilibrium temperature fields that are functions of pressure, rather than σ. So for instance, all grid points at 700hPa are relaxed to the same temperature. This eliminates the diabatic heating over the orography, though new radiative-equilibrium temperature fields have to be generated for each mountain height. The responses in these experiments have very similar patterns to the responses in the original experiments, but are 25 - 50% stronger, depending on the mountain height (e.g., compare panels a and d of Figure 1), suggesting that the radiative heating opposes the orographic forcing and, if anything, damps non-linearities. Whether the diabatic heating that comes from relaxing the zonal-mean temperatures along constant σ-levels is physically realistic or whether the radiative-equilibrium temperature field should be specified along constant pressure surfaces is an open question (see Hu and Boos (2017) for a discussion of the physics of orographic heating in a radiative-convective equilibrium context).

6. Responses to Large Mountains

The stationary EMF convergence, the transient EMF convergence and the friction all have substantial responses in the experiments with large ($H \geq$1km) mountains, while the changes in the mean momentum flux convergence are small (Figure 6). The following subsection discusses the responses of the torque and the stationary EMF convergence, the original terms in the non-acceleration balance, in these experiments, and then subsection b describes the responses of the friction and the transient EMF convergence.

a. Responses of the torque and the stationary EMF convergence

The normalized zonal profiles of the torque and of the stationary EMF convergence are essentially unchanged as H is increased (panels c and e of Figure 6), as the torque decelerates the flow between 30° and 55°N, while the stationary EMFs decelerate the flow between 10° and 35°N and accelerate the flow between 35° and 60°N. As discussed by Lutsko and Held (2016), the torque increases more slowly for these mountains than the H^2 scaling expected from linear theory because of the increased migration of the orographically-forced anticyclone away from the center of the mountain, which causes p_s and $\frac{\partial h}{\partial \lambda}$ to move more strongly out of phase for larger H.

The slower increase of the torque causes the stationary EMF convergence to increase more slowly than expected from linear theory (i.e., more slowly than H^2), however some effect of the increased meridional, versus zonal, propagation of the stationary wave at large mountain heights

(Figure 1a versus Figure 1b) is expected. Intuitively, more meridional propagation should lead to larger normalized stationary EMFs.

Figure 7 confirms this intuition, showing the maximum mountain torque versus the maximum stationary EMF convergence for the GCM experiments[5]. As the inset shows, for small values of H the torque and the stationary EMF convergence nearly follow a one-to-one line, though the maximum stationary EMF convergence is slightly larger, as discussed in the previous section. However, the stationary EMF convergence increases more rapidly than the mountain torque for $H \geq 1$km, so that when $H = 5$km the maximum stationary EMF convergence is $\sim$60% larger than the maximum torque. Hence the increased meridional propagation of the stationary waves in the non-linear regime does lead to increased stationary EMF convergence relative to the torque. The extra stationary EMF convergence must be compensated by the responses of the friction and of the transient EMF convergence.

b. Responses of the friction and the transient EMF convergence

In the $H = 1$km and $H = 2$km experiments there is increased transient EMF convergence north of the mountain and decreased convergence to the south, while the friction is enhanced to the north and reduced to the south (panels b and d Figure 6). These are associated with poleward shifts of the mid-latitude jet (Figure 5). Conversely, the jet shifts equatorwards in the $H = 4$km and $H = 5$km experiments, with the transient EMF convergence reduced north and increased south of the mountain, and the friction having the opposite signed response. The $H = 3$km is intermediate between the 2km and the 4km experiments, though there is a slight equatorward shift of the jet in this case (Figure 5).

[5]The maximums are plotted rather than the meridional integrals because the stationary EMFs decelerate the flow at low latitudes, where the torque is zero.

The filled contours in panels c and e of Figure 8 show the responses of the 350hPa transient EMFs in the H = 2km and H = 4km GCM experiments, respectively. In both simulations, the transient EMFs are enhanced upstream and reduced downstream of the orography. While the regions of enhanced transient EMFs are similar, the downstream reduction of the EMFs is much stronger in the H = 4km experiment, such that there is an increase in the zonal-mean transient EMFs in the 2km experiment and a reduction in the 4km experiment (Figure 8d).

The transient EMFs can be visualized using **E** vectors (Hoskins et al. 1983), which indicate the direction of eddy propagation, and hence the direction of westerly momentum transport. The horizontal components of the **E** vector are given by

$$\mathbf{E_h} = \left(\overline{v'^2 - u'^2}, -\overline{u'v'}\right), \tag{12}$$

and the time-mean $\mathbf{E_h}$ vectors in the control experiment are shown in panel b of Figure 8. In the absence of orography, the eddies primarily propagate to the northeast, leading to northwards momentum transport by transient eddies in the zonal-mean (see panel a of the Figure).

The responses of the $\mathbf{E_h}$ vectors in the H = 2km and H = 4km experiments are shown in panels d and f of Figure 8. In both cases the vectors downstream of the orography primarily point to the southwest, suggesting that the transient eddies are decelerating and also elongating zonally (see Figure 4 of Hoskins et al. (1983)). The region of eddy deceleration and zonal elongation is much larger in the H = 4km experiment than in the H = 2km experiment.

Upstream of the orography, the transient eddies are deflected around the peak of the orography, though unlike the stationary waves, the eddies are deflected equally to the north and to the south of the orography. The jet also widens upstream of the orography in both simulations (black contours in Figure 8c), suggesting that there is more space for meridional eddy propagation. Confirming this, the anomalous **E** vectors southwest of the orography (e.g., near 30°N and 60°E) point to northeast, representing increased polewards transient momentum transport. In the H = 4km experiment, the vectors to the southeast of the orography (i.e., downstream of the orography) point to the southwest, and the jet also narrows in this region. So there is likely to be less space for meridional eddy propagation downstream of the orography, further damping the downstream transient EMFs. It is difficult to see whether this is the case in the H = 2km experiment, and there is also less narrowing of the jet downstream of the orography in this case.

In the H = 2km case the broadening of the jet upstream of the orography, and the larger space for meridional eddy propagation, wins out and the poleward transient EMFs increase compared to the control (Figure 9), pushing the jet polewards. In the H = 4km the deceleration of the eddies downstream of the orography wins out, with evidence of the eddies being disrupted more than 90° downstream of the orography, and the polewards transient EMFs decrease compared to the control (dashed line in Figure 9), favoring an equatorward shift of the jet.

One other potential mechanism by which the orography could cause the jet to shift in latitude is the effect of the locally enhanced baroclinicity on wave-breaking. By enhancing downstream temperature gradients, large-scale orography enhances the local downstream baroclinicity (Son et al. (2009); Lutsko et al. (2019)). This is primarily a result of the stationary eddy heat flux, which fluxes heat into the region southeast of the orography (not shown), increasing the baroclinicity there, as was also seen in the idealized moist GCM simulations of Kaspi and Schneider (2013). Orlanksi (2003) showed that increased low-level baroclinicity favors cyclonic wave-breaking (CWB), which tends to push jets equatorward, rather than anticyclonic wave-breaking (AWB), which tends to push jets poleward. The reason for this is that the amplitude of anticyclonic eddies is bounded by $-f$, because if the absolute vorticity $\zeta + f$ goes to zero then the stretching term in the vorticity equation, which drives the eddies, also goes to zero. By contrast, the amplitude of cyclonic eddies is unbounded, so that as eddy amplitudes increase cyclonic eddies tend to become more prominent relative to anticyclonic eddies.

The wave-breaking algorithm of Rivière (2009) was used to estimate changes in wave-breaking in the control, 2km and 4km simulations. This algorithm identifies and classifies (AWB or CWB) local reversals of the absolute vorticity contours, searching along circumglobal contours whose values are multiples of $10^{-5}s^{-1}$. Only circumglobal contours are considered in order to avoid detecting isolated patches of high or low vorticity that are unrelated to wave-breaking. Applying the wave-breaking algorithm at 250hPa gives AWB:CWB ratios of 1.78±0.01:1 in the control experiment, 1.78±0.02:1 in the 2km experiment and 1.63±0.01:1 in the 4km experiment[6]. In the 4km case then, the locally enhanced baroclinicity downstream of the orography does favor CWB, which may contribute to, or reinforce the equatorward jet shift. In the H = 2km the enhanced baroclinicity does not appear to be sufficient to cause a major change in wave-breaking characteristics.

c. Jet speed

The presence of orography causes the mid-latitude jet to decelerate in all of the experiments, with the deceleration increasing as H is increased (Figure 5). However, the nature of these decelerations differ substantially in the different experiments. In the H = 2km experiment, both the transient and the stationary EMFs decelerate the equatorward flank of the jet, and weakly accelerate the poleward flank (Figure 10d and f). This is balanced by reductions of the friction on the equatorward side of the jet and enhancements on the poleward side of the jet, such that the jet shift is accomplished mostly by a deceleration of the jet equatorwards of roughly 55°N.

[6]Uncertainties were estimated by calculating the AWB:CWB ratios for the first and second halves of the simulations. E.g., the first half of the control simulation gave a ratio of 1.76:1, the second half gave a ratio of 1.80, and using all the data gave 1.78:1.

In the $H = 4$km experiment, the transient and stationary EMFs approximately cancel over most of the orography (Figure 10e and g). Thus the friction must balance the mountain torque (Figure 10i), leading to a strong deceleration in the jet core (where the orography is located). In the subtropics, the response of the transient EMFs is larger than the stationary EMF, causing an acceleration of the jet.

Hence although the jet decelerates in all of the orographic experiments, the reasons are differ considerably in the experiments with smaller ($H \leq$ 2km) and in the larger ($H >$ 2km) experiments. For smaller mountain heights the jet decelerates to compensate for the stationary and transient EMFs, whereas for larger mountains the jet decelerates to balance the mountain torque, with the transient EMFs balancing the stationary EMFs. These cases, then, are far from the balance between stationary EMFs and mountain torque expected from linear theory.

7. Conclusion

This study has used a stationary wave model and an idealized, dry GCM to investigate the impact of orography on the atmosphere's momentum budget, with a focus on assessing the non-acceleration theorem, how transients affect the response to orography and how orography affects the strength and latitude of eddy-driven jets. Comparing simulations with a stationary wave model and a GCM, forced with Gaussian mountains of heights ranging from 0.5m to 5km has produced the following picture of how the two models respond to the presence of orography:

- For the smallest mountain considered here (H = 0.5m) the response of the stationary wave model nearly follows what would be expected from the non-acceleration theorem, as the torque exerted by the mountain on the atmosphere is mostly balanced by the stationary EMF convergence. However, the poleward- and equatorward-propagating wavetrains excited by the orography are dissipated as they propagate away, leading to stationary EMF convergence maxima north and south of the orography, instead of at the latitude of the orography, as well as to stationary EMF divergence in the subtropics. Friction compensates for the residual of the torque and the stationary EMFs.

- A stationary non-linearity develops for larger mountains (H = 10m and higher), caused by the preferential deflection of the flow around the poleward flank of the orography. The non-linearity becomes more prominent as the height of the orography is increased, and causes the primary wave source to shift from being south of the orography to being north of the orography for H = 500m.

- The response of the GCM to small mountains is similar to the stationary wave model, but the transient eddies appear to amplify the stationary non-linearity, and its associated temperature anomalies, leading to a larger response and to larger stationary EMFs. Diabatic heating over the orography, induced by the Newtonian relaxation along constant σ-surfaces, damps the model's response to orography. Whether this heating is physically realistic, or whether studies of orography should instead relax temperatures along constant pressure surfaces is an open question.

- For larger mountains ($H \geq$ 1km), the mountain torque and the stationary EMF increase more slowly than the H^2 scaling suggested by linear theory, though the increasing meridional (as opposed to zonal) propagation of the stationary wave leads to enhanced stationary EMFs relative to the mountain torque. For $H \leq$ 2km the mid-latitude jet shifts polewards, as both the stationary and transient EMFs push the jet poleward. For $H >$ 2km the transient EMFs push the jet equatorward, and balance the stationary EMFs, which always push the jet poleward. The cancellation of the stationary and transient EMFs means that the mountain torque is mostly balanced by the friction, causing the jet to decelerate in its core. For large enough orography, changes in wave-breaking characteristics caused by enhanced downstream baroclinicity may reinforce the jet shift.

- The transient EMFs changes are caused by a competition between the jet widening upstream of the orography, which provides more space for meridional eddy propagation and hence leads to increased poleward transient EMFs upstream of the orography, and the slowdown of the eddies downstream of the orography, such that the transient EMF weakens downstream of the orography. The former effect wins out in the $H = 2$km case, while the latter effect wins out for $H = 4$km. In the $H = 4$km case the jet also narrows downstream of the orography, providing less room for meridional eddy propagation and further damping the transient EMFs.

These results have come in the idealized contexts of a stationary wave model and a dry GCM, but provide several general insights into the impact of orography on the atmosphere's momentum budget, including how the poleward deflection of the flow promotes the development of a stationary non-linearity, even for a mountain with maximum height as small as 10m, and the complex changes in the propagation of transient eddies in the presence of large mountains. Future extensions to this work could explore how the models' responses are affected by moving the orography away from the latitude of maximum wind speeds, the sensitivity of the responses to the shape of the orography (e.g., comparing with meridional and zonal ridges) and how the responses change when the mean flow consists of a double jet (e.g., Son et al. (2009)). Finally, a crucial step for connecting these results to the observed atmosphere is adding the effects of moisture (see Wills and Schneider (2018)).

From a zonal-mean perspective, the non-acceleration theorem is the starting point for thinking about the atmosphere's response to orography, but a complete theory requires accounting for a number of other factors, including friction, transients and interactions between eddy-driven jets and stationary waves. Systematically investigating how these factors combine to determine the response to orography across a hierarchy of models of different complexity, for a wide range of mountain heights, is essential for deepening our understanding of large-scale orography's role in shaping the observed circulation of the atmosphere, and of orography's role in past and future climates.

APPENDIX

A1. Plumb Fluxes

The horizontal and vertical components of the Plumb flux are calculated as (Plumb 1985):

$$\mathbf{PF} = \begin{pmatrix} PF_x \\ PF_y \\ PF_z \end{pmatrix} = \begin{pmatrix} \frac{1}{2a^2\cos\phi}\left(\frac{\partial \psi'}{\partial \lambda}^2 - \psi'\frac{\partial^2 \psi'}{\partial \lambda^2}\right) \\ \frac{1}{2a}\left(\frac{\partial \psi'}{\partial \lambda}\frac{\partial \psi'}{\partial \phi} - \psi'\frac{\partial \psi'}{\partial \phi \partial \lambda}\right) \\ \frac{p}{1000\mathrm{hPa}} f\cos\phi\left(\frac{\partial [\overline{\theta}]}{\partial z}\right)^{-1}\left([v^*\theta^*] - \frac{[\psi^*]}{a\cos\phi}\frac{\partial [\theta^*]}{\partial \lambda}\right) \end{pmatrix} \quad \text{(A1)}$$

with θ denoting potential temperature and all other symbols having the same meaning as in the main text.

Acknowledgment. I thank Isaac Held for suggestions and comments on early stages of this project, and two reviewers for thorough readings and helpful comments.

References

Andrews, D. G., and M. E. McIntyre, 1976: Planetary waves in horizontal and vertical shear: The generalized eliassen-palm relation and the mean zonal acceleration. *Journal of the Atmospheric Sciences*, **33**, 2031–2048.

Brandefelt, J., and H. Kornich, 2008: Northern hemisphere stationary waves in future climate projections. *Journal of Climate*, **21 (23)**, 6341–6353.

Branstator, G., 1983: Horizontal energy propagation in a barotropic atmosphere with meridional and zonal structure. *Journal of the Atmospheric Sciences*, **40 (7)**, 1689–1708.

Branstator, G., 2002: Circumglobal teleconnections, the jet stream waveguide, and the north atlantic oscillation. *Journal of Climate*, **15 (14)**, 1893–1910.

Branstator, G., and F. Selten, 2009: 'modes of variability' and climate change. *Journal of Climate*, **22 (10)**, 2639–2658.

Brayshaw, D. J., B. Hoskins, and M. Blackburn, 2009: The basic ingredients of the north atlantic storm track. part i: Landsea contrast and orography. *Journal of the Atmospheric Sciences*, **66 (14)**, 2539–2558.

Chang, E. K. M., 2009: Diabatic and orographic forcing of northern winter stationary waves and storm tracks. *Journal of Climate*, **22 (14)**, 670–688.

Charney, J. G., and J. G. DeVore, 1979: Multiple flow equilibria in the atmosphere and blocking. *Journal of the Atmospheric Sciences*, **36 (7)**, 1205–1216.

Charney, J. G., and A. Eliassen, 1949: A numerical method for predicting the perturbations of the middle latitude westerlies. *Tellus*, **1 (2)**, 38–54.

Cook, K. H., and I. M. Held, 1992: The stationary response to large-scale orography in a general circulation model and a linear model. *Journal of the Atmospheric Sciences*, **49 (6)**, 525–539.

Derome, J., and A. Wiin-Nielsen, 1971: The response of a middle-latitude model atmosphere to forcing by topography and stationary heat sources1,,2. *Monthly Weather Review*, **99 (7)**, 564–576.

Egger, J., 1978: Dynamics of blocking highs. *Journal of the Atmospheric Sciences*, **35 (10)**, 1788–1801.

Grose, W. L., and B. J. Hoskins, 1979: On the influence of orography on large-scale atmospheric flow. *Journal of the Atmospheric Sciences*, **36 (2)**, 223–234.

Held, I. M., 1983: Stationary and quasi-stationary eddies in the extratropical troposphere: theory. *Large-scale Dynamical Processes in the Atmosphere*, B. J. Hoskins, and R. P. Pearce, Eds., Academic Press, New York, NY.

Held, I. M., and M. J. Suarez, 1994: A proposal for the intercomparison of the dynamical cores of atmospheric general circulation models. *Bulletin of the American Meteorological Society*, **75 (10)**, 1825–1830.

Held, I. M., M. Ting, and H. Wang, 2002: Northern winter stationary waves: Theory and modeling. *Journal of Climate*, **15 (16)**, 2125–2144.

Hoskins, B. J., and T. Ambrizzi, 1993: Rossby wave propagation on a realistic longitudinally varying flow. *Journal of the Atmospheric Sciences*, **50 (12)**, 1661–1671.

Hoskins, B. J., I. N. James, and G. H. White, 1983: The shape, propagation and mean-flor interaction of large-scale weather systems. *Journal of the Atmospheric Sciences*, **40 (7)**, 1595–1612.

Hoskins, B. J., and D. J. Karoly, 1981: The steady linear response of a spherical atmosphere to thermal and orographic forcing. *Journal of the Atmospheric Sciences*, **38 (6)**, 1179–1196.

Hoskins, B. J., A. J. Simmons, and D. G. Andrews, 1977: Energy dispersion in a barotropic atmosphere. *Quarterly Journal of the Royal Meteorological Society*, **103 (438)**, 553–567.

Hu, S., and W. R. Boos, 2017: The Physics of Orographic Elevated Heating in RadiativeConvective Equilibrium. *Journal of the Atmospheric Sciences*, **74 (9)**, 2949–2965.

Kasahara, A., 1966: The dynamical influence of orography on the large-scale motion of the atmosphere. *Journal of the Atmospheric Sciences*, **23 (3)**, 259–271.

Kaspi, Y., and T. Schneider, 2013: The Role of Stationary Eddies in Shaping Midlatitude Storm Tracks. *Journal of the Atmospheric Sciences*, **70 (8)**, 2596–2613.

Killworth, P. D., and M. E. McIntyre, 1985: Do rossby-wave critical layers absorb, reflect, or over-reflect? *Journal of Fluid Mechanics*, **161**, 449–492.

Lutsko, N. J., J. W. Baldwin, and T. W. Cronin, 2019: The impact of large-scale orography on northern hemisphere winter synoptic temperature variability. *Journal of Climate*, **32 (18)**, 5799–5814.

Lutsko, N. J., and I. M. Held, 2016: The response of an idealized atmosphere to orographic forcing: Zonal versus meridional propagation. *Journal of the Atmospheric Sciences*, **73 (7)**, 3701–3718.

Manabe, S., and T. B. Terpstra, 1974: The effects of mountains the general circulation of the atmosphere as identified by numberical experiments. *Journal of the Atmospheric Sciences*, **31 (14)**, 3–42.

Manola, I., F. Selten, H. de Vries, and W. Hazeleger, 2013: waveguidability of idealized jets. *Journal of Geophysical Research: Atmospheres*, **118 (18)**, 10,432–10,440.

Nigam, S., I. M. Held, and S. W. Lyons, 1988: Linear simulation of the stationary eddies in a GCM. part II: The mountain model. *Journal of the Atmospheric Sciences*, **45 (9)**, 1433–1452.

Orlanksi, I., 2003: Bifurcation in eddy life cycles: Implications for storm track variability. *Journal of the Atmospheric Sciences*, **60 (14)**, 993–1023.

Park, H.-S., S.-P. Xie, and S.-W. Son, 2013: Poleward stationary eddy heat transport by the tibetan plateau and equatorward shift of westerlies during northern winter. *Journal of the Atmospheric Sciences*, **70 (23)**, 3288–3301.

Peixoto, J. P., and A. H. Oort, 1992: *Physics of Climate*. 1st ed., Springer-Verlag, New York, USA.

Petoukhov, V., S. Rahmstorf, S. Petri, and H. J. Schellnhuber, 2013: Quasiresonant amplification of planetary waves and recent northern hemisphere weather extremes. *Proceedings of the National Academy of Sciences*, **110 (14)**, 5336–5341.

Plumb, R. A., 1985: On the three-dimensional propagation of stationary waves. *Journal of the Atmospheric Sciences*, **42 (3)**, 217 – 229.

Rivière, G., 2009: Effect of Latitudinal Variations in Low-Level Baroclinicity on Eddy Life Cycles and Upper-Tropospheric Wave-Breaking Processes. *Journal of the Atmospheric Sciences*, **66 (6)**, 1569–1592.

Saeed, S., N. Van Lipzig, W. A. Muller, F. Saeed, and D. Zanchettin, 2014: Influence of the circumglobal wave-train on european summer precipitation. *Climate Dynamics*, **43**, 503–515.

Saltzman, B., 1963: A generalized solution for the large-scale, time-average perturbations in the atmosphere. *Journal of the Atmospheric Sciences*, **20 (3)**, 226–235.

Saltzman, B., 1965: On the theory of the winter-average perturbations in the troposphere and stratosphere. *Monthly Weather Review*, **93 (4)**, 195–211.

Sandu, I., and Coauthors, 2019: Impacts of orography on large-scale atmospheric circulation. *npj Climate and Atmospheric Science*, **2 (1)**, 1–10.

Simpson, I. R., R. Seager, M. Ting, and T. A. Shaw, 2016: Causes of change in Northern Hemisphere winter meridional winds and regional hydroclimate. *Nature Climate Change*, **6 (1)**, 65–70.

Smagorinsky, J., 1953: The dynamical influence of large-scale heat sources and sinks on the quasi-stationary mean motions of the atmosphere. *Quarterly Journal of the Royal Meteorological Society*, **79 (341)**, 342–366.

Son, S.-W., M. Ting, and L. M. Polvani, 2009: The effect of topography on storm-track intensity in a relatively simple general circulation model. *Journal of the Atmospheric Sciences*, **66 (23)**, 393–311.

Trenberth, K. E., and S. C. Chen, 1988: Planetary waves kinematically forced by himalayan orography. *Journal of the Atmospheric Sciences*, **45 (20)**, 2934–2948.

Valdes, P. J., and B. J. Hoskins, 1991: Nonlinear orographically forced planetary waves. *Journal of the Atmospheric Sciences*, **(18)**, 2089–2106.

Vallis, G. K., and J. O. Roads, 1984: Large-scale stationary and turbulent flow over topography. *Journal of the Atmospheric Sciences*, **41 (14)**, 3255–3270.

Walker, C. C., and G. Magnusdottir, 2003: Nonlinear planetary wave reflection in an atmospheric GCM. *Journal of the Atmospheric Sciences*, **60 (2)**, 279–286.

Wang, L., and P. J. Kushner, 2010: Interpreting stationary wave nonlinearity in barotropic dynamics. *Journal of the Atmospheric Sciences*, **67 (7)**, 2240–2250.

White, A. A., 1986: Finite amplitude, steady rossby waves and mean flows: Analytical illustrations of the charney-drazin non-acceleration theorem. *Quarterly Journal of the Royal Meteorological Society*, **112**, 749–773.

White, R. H., D. S. Battisti, and G. H. Roe, 2017: Mongolian Mountains Matter Most: Impacts of the Latitude and Height of Asian Orography on Pacific Wintertime Atmospheric Circulation. *Journal of Climate*, **30 (11)**, 4065–4082.

Wills, R. C. J., and T. Schneider, 2018: Mechanisms Setting the Strength of Orographic Rossby Waves across a Wide Range of Climates in a Moist Idealized GCM. *Journal of Climate*, **31 (18)**, 7679–7700.

LIST OF FIGURES

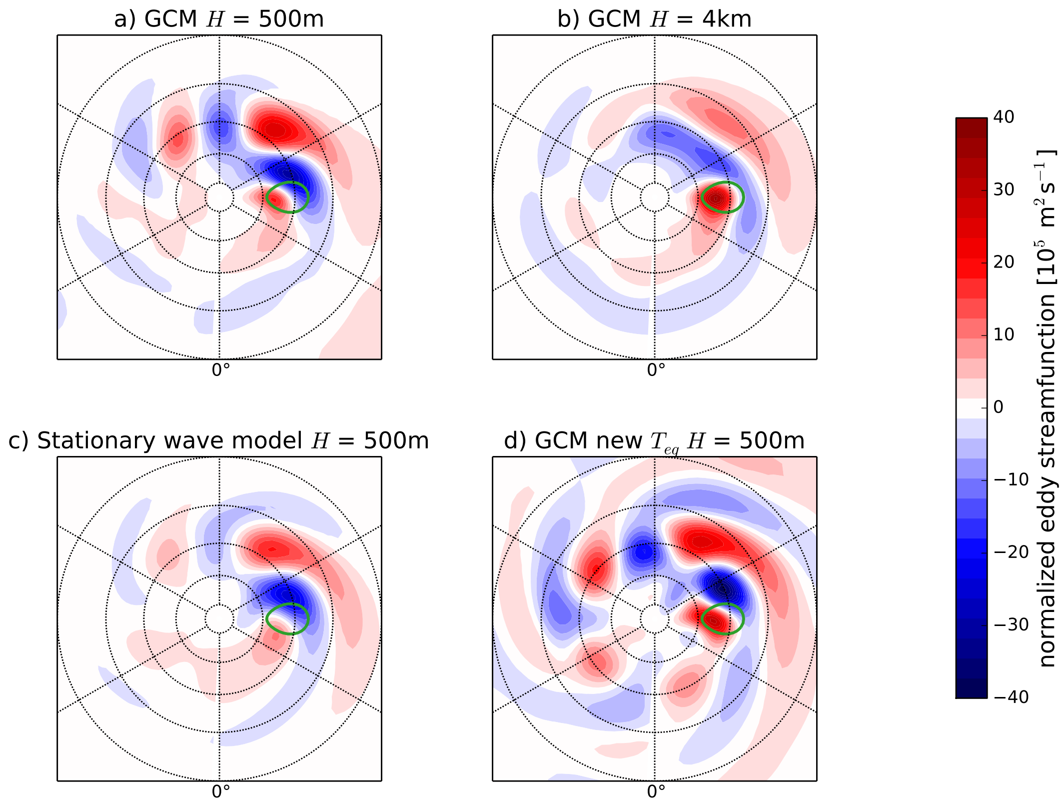

FIG. 1. a) The GCM's eddy streamfunction response at 350hPa, normalized by 1/H for the experiment with H = 500m. b) Same but for the GCM experiment with H = 4km. c) The normalized eddy streamfunction response at 350hPa for the stationary wave model experiment with H = 500m. d) The normalized eddy streamfunction at 350hPa for the GCM experiment with H = 500m and a new equilibrium temperature field defined along constant pressure surfaces.

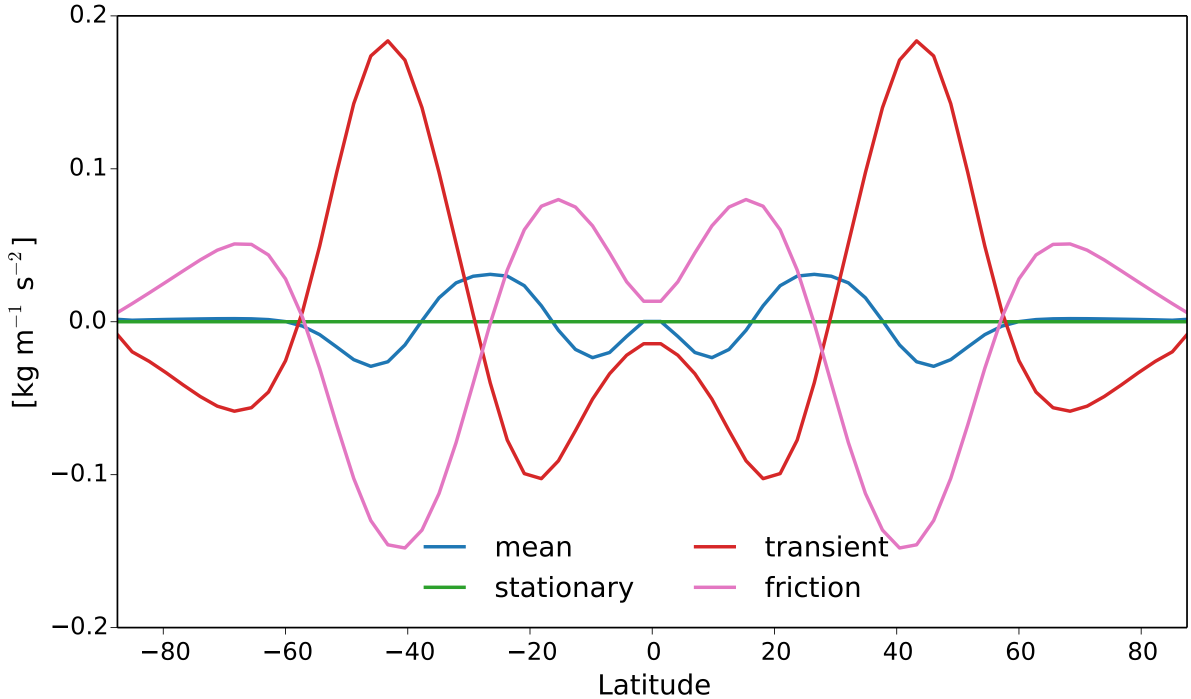

FIG. 2. Vertically-integrated terms in the zonal-mean momentum budget (equation 11) of the control simulation.

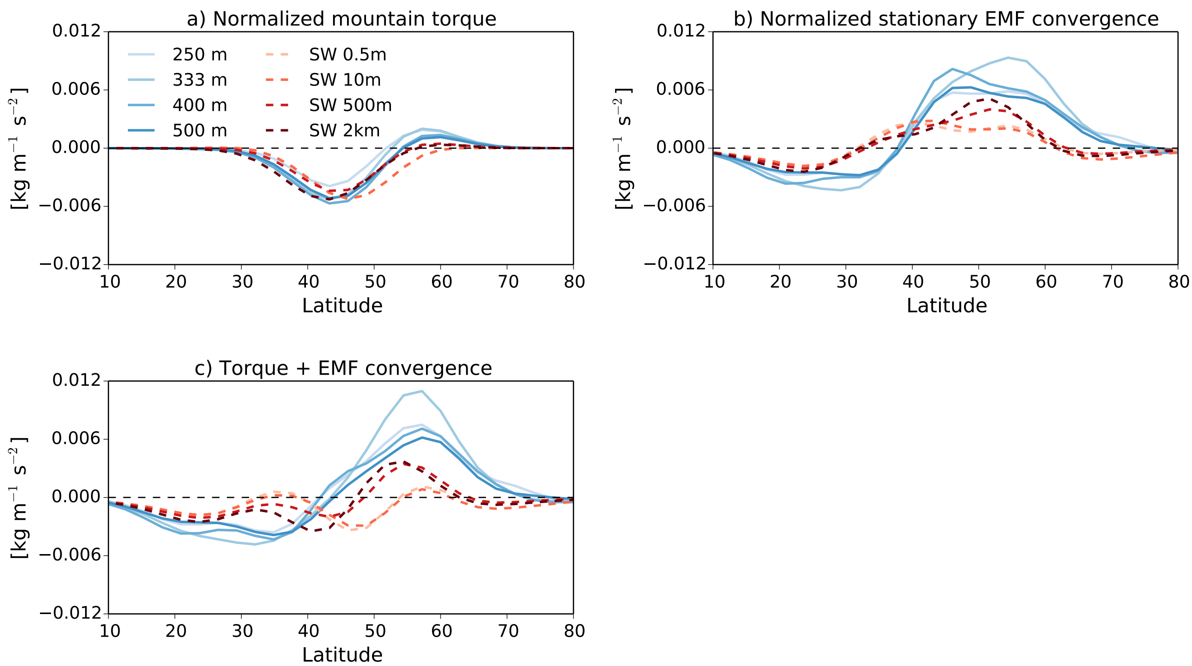

FIG. 3. The normalized mountain torque (panel a), the convergence of the normalized stationary EMF (panel b) and the sum of these (panel c) for the GCM experiments in the linear regime ($H < 1$km, blue lines) and for the stationary wave model experiments (dashed red lines).

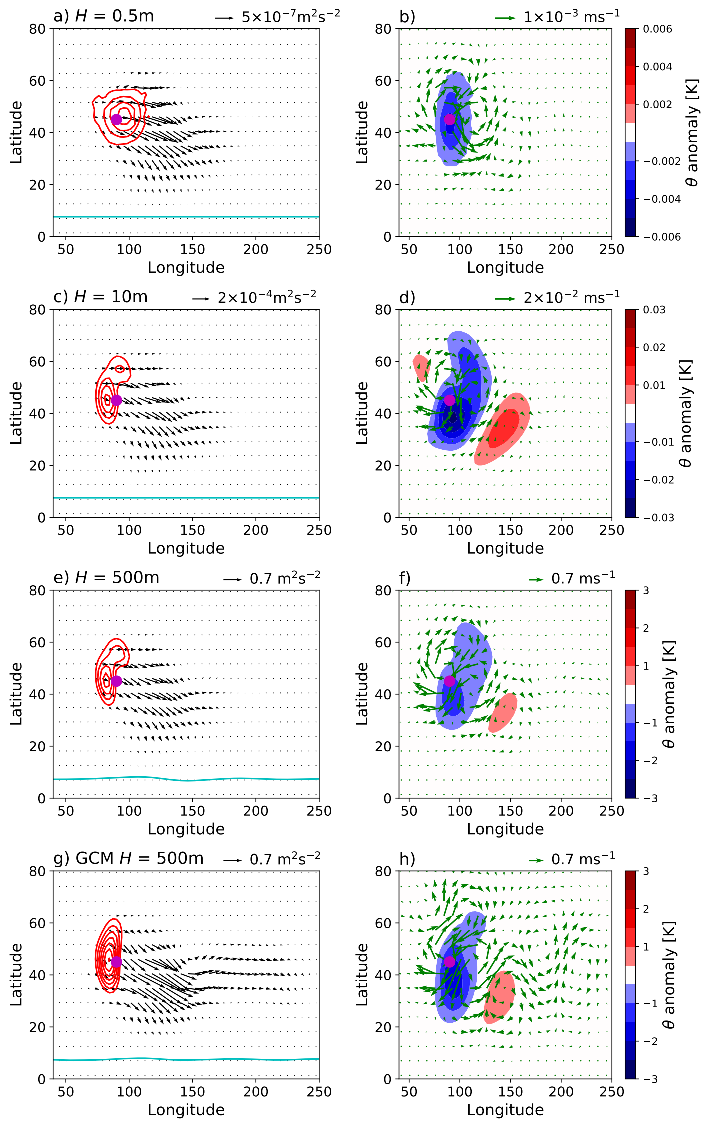

FIG. 4. a) Horizontal components of Plumb flux at 350hPa (arrows) and vertical component of Plumb flux at 800hPa (red contours, contour interval = 2×10^{-9}m^{2}s^{-2}, smallest contour = 2×10^{-9}m^{2}s^{-2}) for the stationary wave simulation with H = 0.5m. The cyan lines shows the critical line where $u = 0$ and the purple circle marks the center of the orography. b) Horizontal wind vectors at 800hPa (green arrows) and eddy potential temperature at 800hPa (filled contours) for the stationary wave simulation with H = 0.5m. c) Same as panel a) but for the experiment with H = 10m (and new contour interval = 5×10^{-7}m^{2}s^{-2}, smallest contour = 1×10^{-6}m^{2}s^{-2}). d) Same as b) but for the experiment with H = 10m. e) Same as panel a) but for the experiment with H = 10m (and new contour interval = 2×10^{-3}m^{2}s^{-2}, smallest contour = 4×10^{-3}m^{2}s^{-2}). f) Same as b) but for the experiment with H = 10m. g) Same as panel e) but for the GCM simulation with H = 500m. h) Same as panel f) but for the GCM simulation with H = 500m.

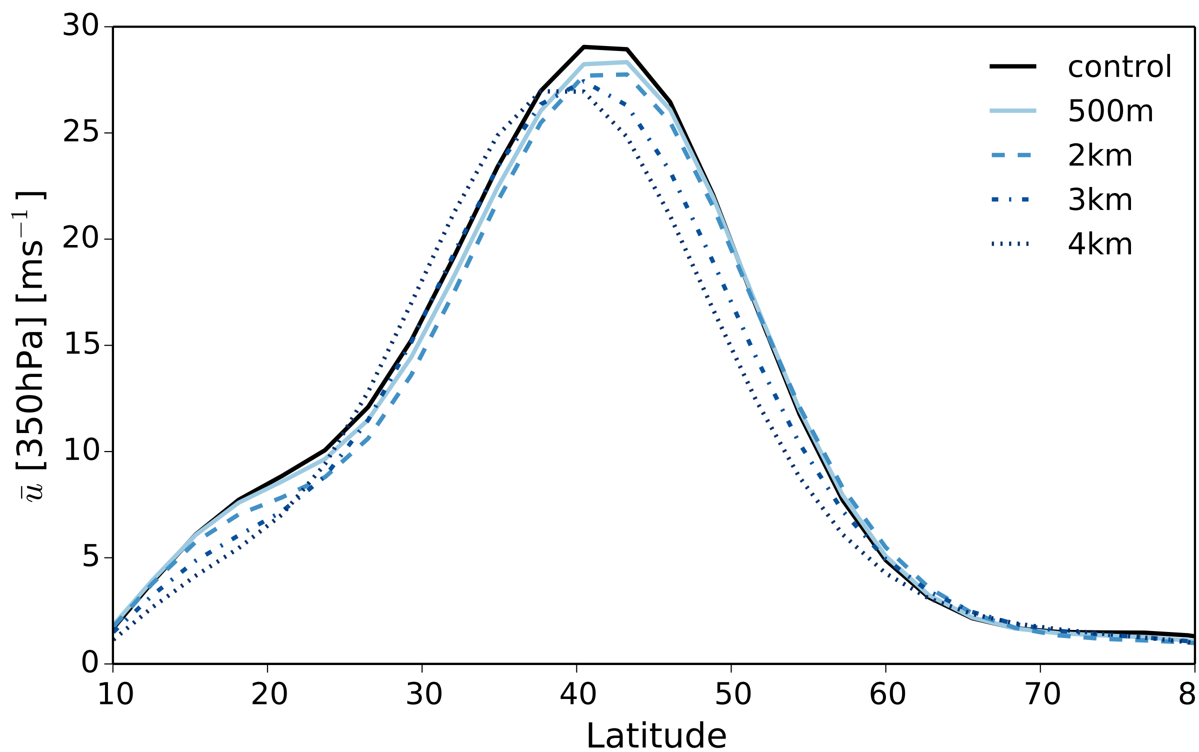

FIG. 5. 350hPa zonal-mean wind in the control GCM experiment (black line), the H = 500m experiment (solid blue line), the H = 2km experiment (dashed blue line) and the H = 4km experiment (dotted blue line).

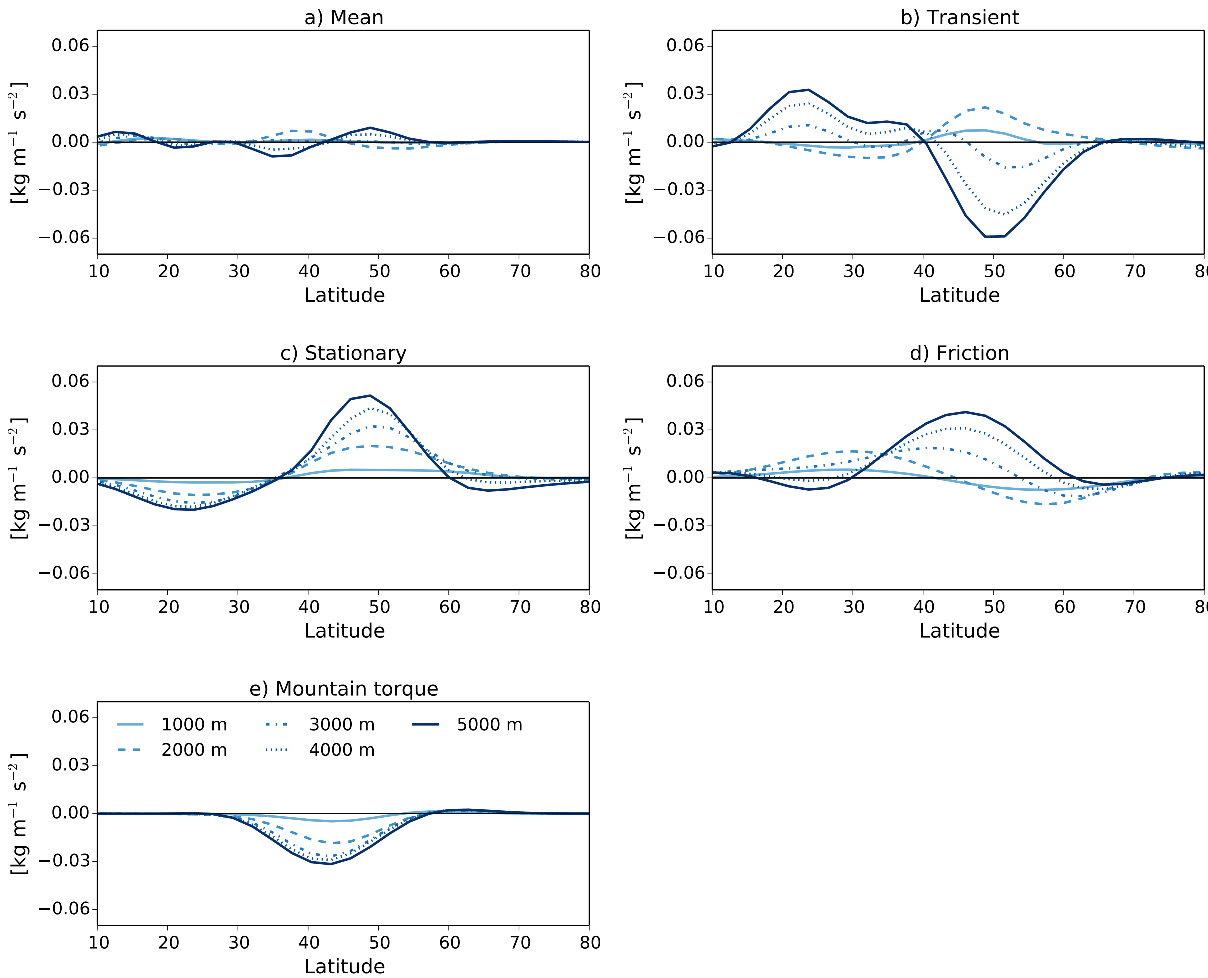

FIG. 6. Responses of the terms in the momentum budget (equation 11) to mountains with $H \geq$1km.

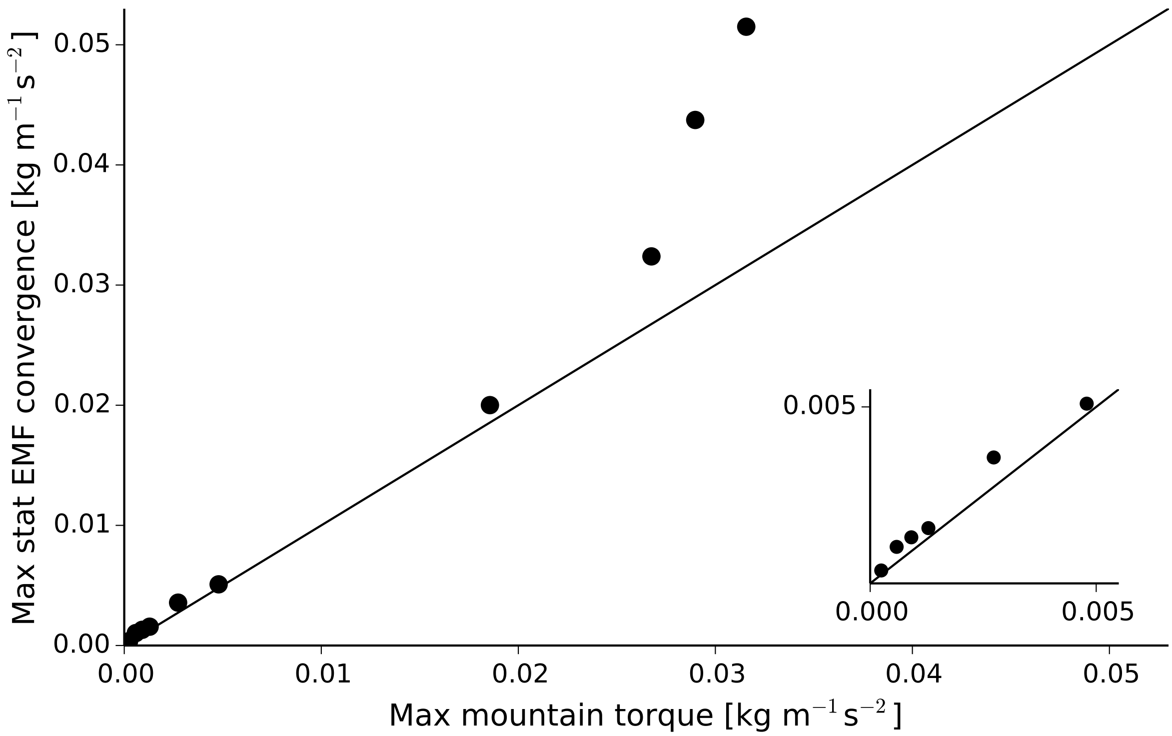

FIG. 7. The maximum stationary EMF convergence versus the maximum mountain torque in the GCM experiments. The straight line plots a one-to-one fit and the inset shows a close-up of the six smallest mountains ($H \leq$1km).

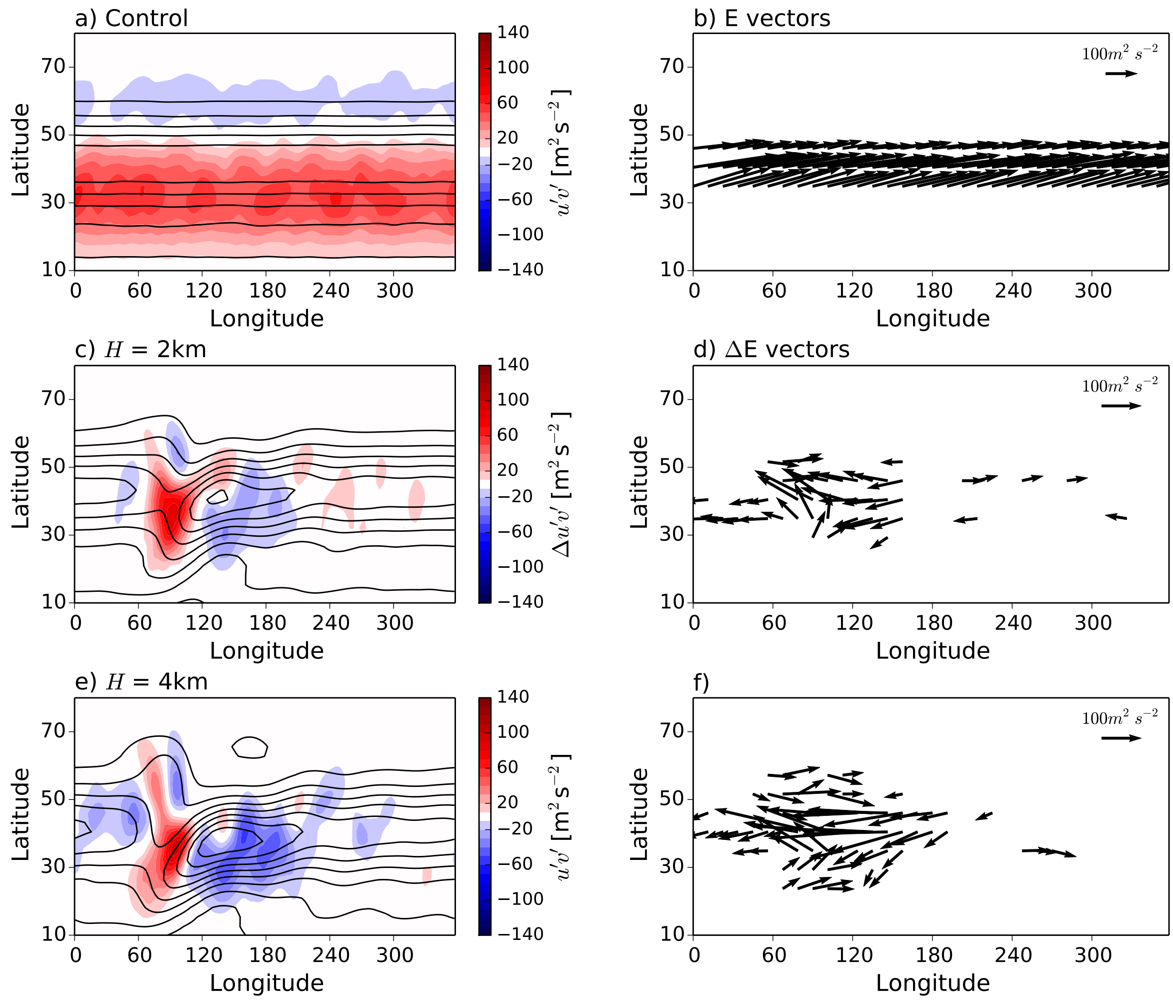

FIG. 8. a) 350hPa transient EMFs (filled contours) and 350hPa zonal winds (black contours) in the control GCM experiment. b) Horizontal components of the **E** vectors at 350hPa in the control experiment. c) 350hPa zonal winds (black contours) in the H = 2km experiment and change in the 350hPa transient EMFs in the H = 2km GCM experiment relative to the control experiment (filled contours). d) Response of the horizontal components of the **E** vectors at 350hPa in the H = 2km experiment. e) 350hPa zonal winds (black contours) in the H = 4km experiment and change in the 350hPa transient EMFs in the H = 4km GCM experiment relative to the control experiment (filled contours). f) Response of the horizontal components of the **E** vectors at 350hPa in the H = 4km experiment. The contour interval for the zonal-wind in panels a, c and e is 5 ms^{-1}.

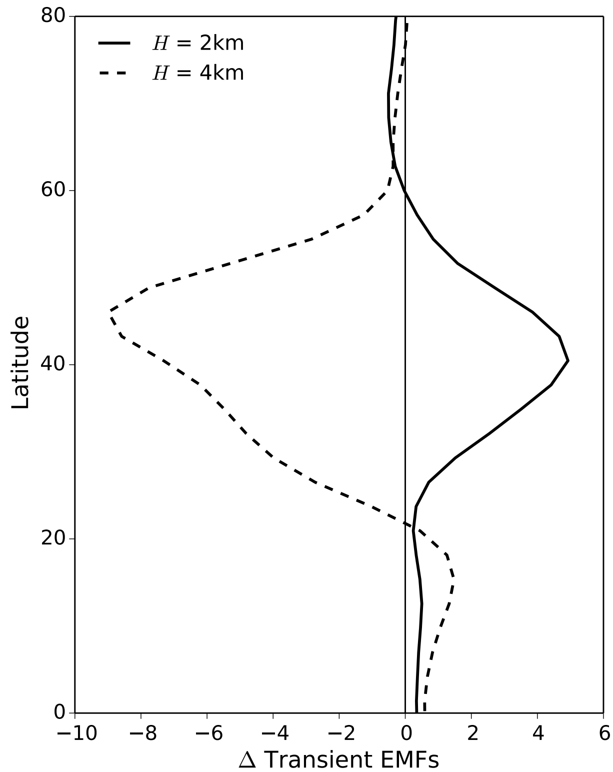

FIG. 9. Responses of the zonal-mean 350hPa transient EMFs in the H = 2km experiment (solid black line) and in the H = 4km experiment (dashed black line) relative to the control experiment.

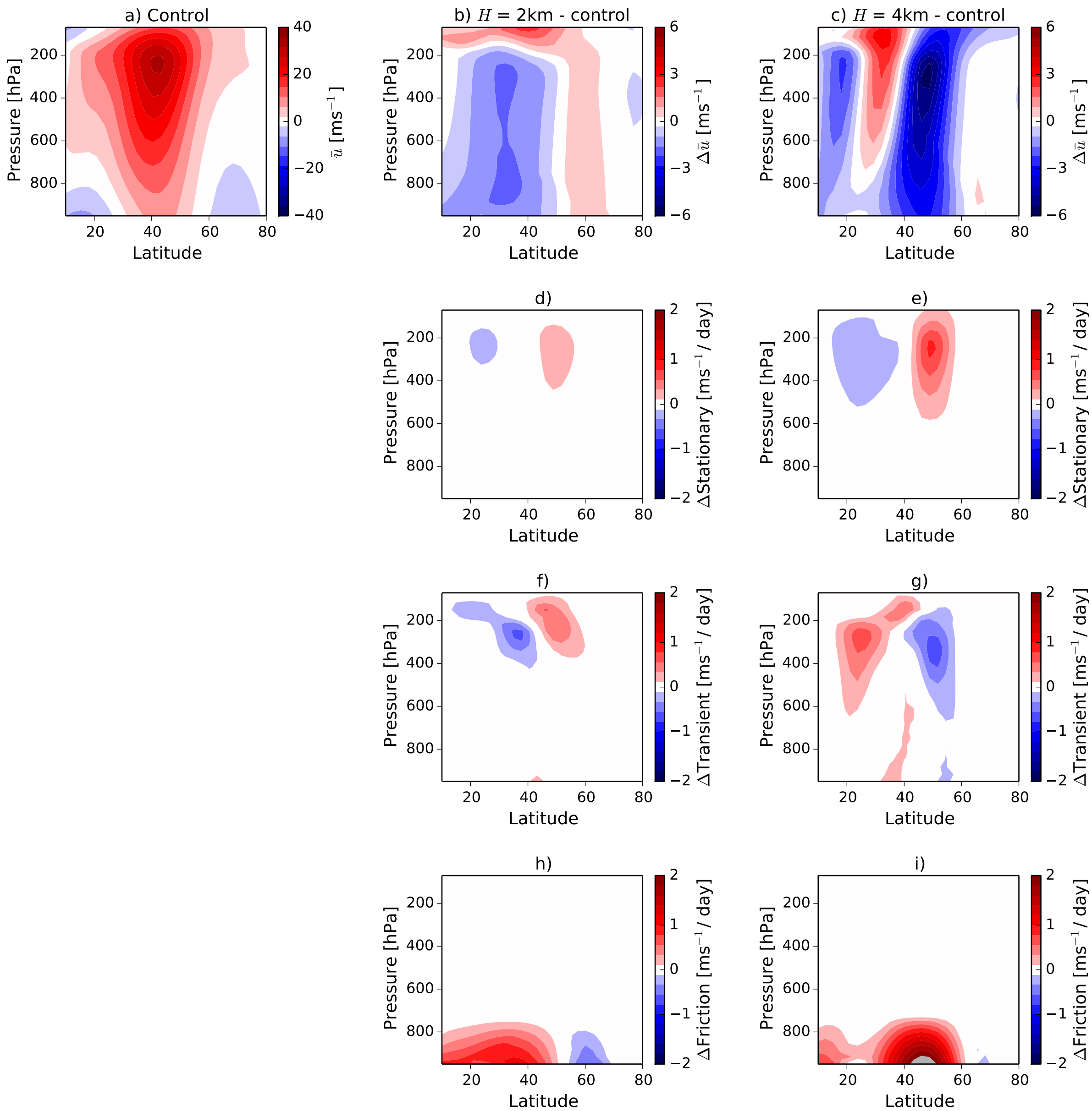

FIG. 10. a) Pressure-latitude profile of the zonal-mean winds in the control GCM experiment. b) Response of the zonal-mean winds in the H = 2km experiment. c) As in panel b), but for the H = 4km experiment. d) Response of the zonal-mean stationary EMF convergence in the H = 2km experiment. e) As in panel d), but for the H = 4km experiment. f) Response of the zonal-mean transient EMF convergence in the H = 2km experiment. g) As in panel f), but for the H = 4km experiment. h) Response of the zonal-mean friction in the H = 2km experiment. i) As in panel h), but for the H = 4km experiment.